Vibrio cholerae biofilm growth program and architecture revealed by single-cell live imaging

Jing Yan[a,b], Andrew G. Sharo[c], Howard A. Stone[a], Ned S. Wingreen[b], and Bonnie L. Bassler[b,d,1]

[a]Department of Mechanical and Aerospace Engineering, Princeton University, Princeton, NJ 08544; [b]Department of Molecular Biology, Princeton University, Princeton, NJ 08544; [c]Department of Physics, Princeton University, Princeton, NJ 08544; and [d]Howard Hughes Medical Institute, Chevy Chase, MD 20815

Contributed by Bonnie L. Bassler, July 18, 2016 (sent for review July 3, 2016; reviewed by George O'Toole and Joao B. Xavier)

Biofilms are surface-associated bacterial communities that are crucial in nature and during infection. Despite extensive work to identify biofilm components and to discover how they are regulated, little is known about biofilm structure at the level of individual cells. Here, we use state-of-the-art microscopy techniques to enable live single-cell resolution imaging of a *Vibrio cholerae* biofilm as it develops from one single founder cell to a mature biofilm of 10,000 cells, and to discover the forces underpinning the architectural evolution. Mutagenesis, matrix labeling, and simulations demonstrate that surface adhesion-mediated compression causes *V. cholerae* biofilms to transition from a 2D branched morphology to a dense, ordered 3D cluster. We discover that directional proliferation of rod-shaped bacteria plays a dominant role in shaping the biofilm architecture in *V. cholerae* biofilms, and this growth pattern is controlled by a single gene, *rbmA*. Competition analyses reveal that the dense growth mode has the advantage of providing the biofilm with superior mechanical properties. Our single-cell technology can broadly link genes to biofilm fine structure and provides a route to assessing cell-to-cell heterogeneity in response to external stimuli.

biofilm | single cell | self-organization | community | biomechanics

Biofilms are surface-associated bacterial communities embedded in an extracellular matrix (1–3). Biofilm cells are more resistant to antibiotics than their planktonic counterparts, which is a major problem in the context of chronic infections (4, 5). Also, bacterial biofilms clog networks and filters in industrial settings (6). On the other hand, biofilms can be useful, for example, in waste-water treatment (7). Investigations have focused on the genetic and regulatory features driving biofilm formation and on defining the composition of the extracellular matrix (8). However, still lacking is a fundamental biophysical understanding of how bacteria, in time and space, build these 3D structures that attach to surfaces and resist mechanical and chemical perturbations. One common assumption is that bacteria produce polymeric matrices that expand the volume occupied by cells and carry them into the third dimension, as demonstrated by many computer simulations (9, 10). Matrix proteins, extracellular DNA, lipids, and bacteriophages have also been shown to influence the formation of the overall biofilm structure (8). However, the role the bacterial cells themselves play in shaping the biofilm architecture has not been widely investigated; hence, many basic questions remain. For example, for rod-shaped cells that initially attach parallel to a surface, how is 3D growth possible, given the directional division of the cells? How does the arrangement of individual cells determine the global architecture of the biofilm? The inability to answer these and other basic questions stems from a lack of understanding of the cellular-scale architecture of biofilms, which, in turn, highlights a lack of technology capable of tracking the time evolution of biofilms at the single-cell level, in stark contrast to the established tools available for analogous studies of development in eukaryotic organisms (11). Despite tremendous progress in imaging biofilms (12), bottlenecks remain due to resolution and phototoxicity issues. Thus, our understanding of biofilms primarily comes from high-resolution optical images of immature biofilms that are only a few cell layers thick (13), low-resolution images of the 3D contour (12), or electron microscopy images of processed samples (14), which lack the key spatiotemporal information required to understand the biofilm developmental process at the level of the basic unit: the individual cell.

Here, we succeed in imaging living, growing biofilms with single-cell resolution and use this ability to discover how biological and physical factors combine to drive the construction of bacterial biofilms. We use *Vibrio cholerae*, the bacterium responsible for the pandemic disease cholera as our model organism. Biofilm formation is a key feature in the *V. cholerae* pathogenic and environmental lifestyles (15). Earlier studies defined regulatory and matrix components that are crucial for proper *V. cholerae* biofilm formation (16). In addition to extracellular polysaccharide (Vps), the matrix protein RbmA (rugosity and biofilm structure modulator A) binds mother-daughter cells together at their poles, Bap1 (biofilm-associated protein 1) adheres cells to the surface, and RbmC/Bap1 forms an envelope around cell subclusters in conjunction with Vps (17). The expression of the genes encoding these components is controlled by intracellular cyclic-diguanylate (c-di-GMP) levels and by quorum sensing (18, 19). Beyond these overarching principles, it is not known how *V. cholerae* builds a biofilm cell by cell. Using live single-cell resolution imaging combined with mutagenesis and in situ matrix labeling, we discover that the directional proliferation of the rod-shaped bacterial cells is the main driving force influencing the overall architecture of the biofilm. We also define how the different matrix proteins contribute distinctly to this process. Finally, we perform fitness and competition analyses to reveal the

Significance

Biofilms are surface-associated bacterial communities embedded in an extracellular matrix. Connections between biofilm architectural, material, and mechanical features have never been systematically studied at the individual cell level due to inadequate optical resolution. Here, we develop imaging, experimental, and modeling tools to analyze living, growing bacterial biofilms at single-cell resolution. We discover that *Vibrio cholerae* biofilms undergo a 2D-to-3D transition as a consequence of directional cell division and anisotropic pressure caused by cell-to-surface adhesion. Moreover, deletion of a single gene responsible for cell-to-cell adhesion changes the biofilm growth mode from directional cell growth to expansion caused by the extracellular matrix. The technology reported here enables future studies of single-cell gene expression in bacterial communities.

Author contributions: J.Y., A.G.S., H.A.S., N.S.W., and B.L.B. designed research; J.Y. and A.G.S. performed research; J.Y. contributed new reagents/analytic tools; J.Y., A.G.S., H.A.S., N.S.W., and B.L.B. analyzed data; and J.Y., A.G.S., H.A.S., N.S.W., and B.L.B. wrote the paper.

Reviewers: G.O., Dartmouth Medical School; and J.B.X., Memorial Sloan–Kettering.

Conflict of interest statement: J.B.X. and B.L.B. were coauthors on a multi-author/multi-institution perspective published in 2012. They have not collaborated scientifically, nor do they have any grants together.

[1]To whom correspondence should be addressed. Email: bbassler@princeton.edu.

This article contains supporting information online at www.pnas.org/lookup/suppl/doi:10.1073/pnas.1611494113/-/DCSupplemental.

evolutionary advantage of the dense, final architecture versus other possible architectures.

Results and Discussion

Single-Cell Live Imaging Reveals Ordering. We and others recently reported single-cell resolution imaging of fixed bacterial biofilm samples using staining and ensemble averaging (20, 21). Because these analyses relied on fixed cells, they could not uncover key temporal information about the biofilm developmental process. Therefore, our first goal in the present work was to advance the field by achieving single-cell imaging of living, growing biofilms. To accomplish this goal, we optimized a customized spinning disk confocal microscope, integrated the gene encoding the highly fluorescent and photostable protein mKO as a constitutive reporter into the *V. cholerae* genome (22), and developed an imaging procedure using minimum laser exposure and adaptive z ranges to reduce phototoxicity to the cells and photobleaching of the chromophores (*Materials and Methods*). We studied a commonly used rugose variant (denoted Rg) of *V. cholerae* that forms robust biofilms due to increased production of c-di-GMP (23). We seeded sample chambers at low cell density so that we could follow the development of isolated biofilm clusters from single founder cells to 10,000 cells (Fig. 1 *A–D* and Movies S1 and S2) at a temporal resolution of one cell-division cycle (≈30 min), using static 96-well chambers. The raw data show that cell clusters initially expand radially in a branched pattern primarily in two dimensions, but subsequently transition into dense 3D domes. Strikingly, in mature biofilms, the central core harbors cells aligned side-by-side oriented vertically to the surface, whereas cells at the periphery align radially and remain horizontal relative to the surface.

To quantify spatial heterogeneity in cell ordering, we deconvolved the z-stack images and segmented the entire biofilm cluster into individual cells using semiautomated, home-written image analysis codes (Fig. 1*E* and Fig. S1). We define four parameters (Fig. 1*F*): e_z and e_r, the z and radial components of each cell's orientation director, respectively; ϕ, the volume fraction of cells in space; and ζ, the cell-to-cell alignment parameter, defined as the absolute value of the cosine of the angle between neighboring cells, all averaged locally within a given region. The ϕ plot shows that the cluster has a roughly hemispherical shape with a dense core. The term e_z captures the vertically aligned central core that begins forming around 14 h after biofilm initiation (Fig. S2 and Movie S3). By contrast, e_r shows that the cells located at the periphery are radially aligned throughout the entirety of biofilm growth. The ζ plot demonstrates that cells at the center of a mature cluster are aligned parallel to each other, indicating a high nematic order (24).

To define the global features of a growing biofilm cluster during development, we plotted four spatially averaged parameters versus time (Fig. 1*G*) for a single cluster. The total cell number initially increases exponentially, but subsequently slows before entrance into stationary phase. The growth curve of biofilm cells is similar to the growth curve of their planktonic counterparts. The averaged orientation of the cells in the center of the cluster evolves from a horizontal ($\langle e_z \rangle = 0$) to vertical orientation ($\langle e_z \rangle \sim 0.7$) consistent with observations in Fig. 1 *A–D*. V_{cell}, the effective biovolume per cell, characterizes the compactness of the cell cluster and shows three characteristic phases. In phase I, the steady increase in V_{cell} captures the 2D branched growth pattern. In phase II, V_{cell} decreases, indicating that the cells proliferate within a confined space in this phase. Notably, this

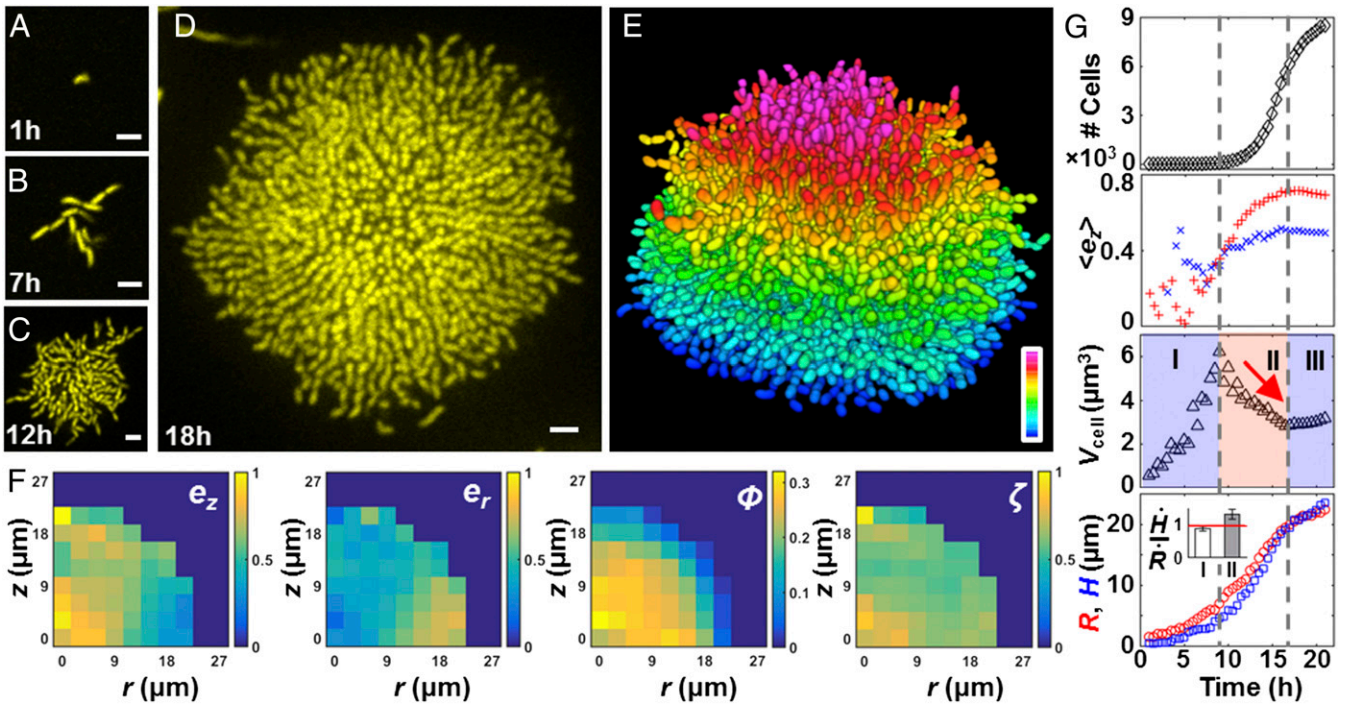

Fig. 1. Single-cell imaging of a growing *V. cholerae* biofilm cluster. Cross-sectional images of the bottom cell layer at 1 h (*A*), 7 h (*B*), 12 h (*C*), and 18 h (*D*). (Scale bars: 3 μm.) (*E*) Segmenting the 3D biofilm cluster in *D* into 7,199 cells, color-coded according to z position (0–21 μm). (*F*) Spatial distribution of the z and radial components of each cell's orientation director e_z and e_r, volume fraction ϕ, and alignment order parameter ζ for the 18-h cluster in *E*. (*G*) Time evolution of cell number, averaged e_z, biovolume per cell V_{cell}, cluster radius R (red circles), and height H (blue squares). In the e_z plot, average values from cells with x–y coordinates that are less and more than $R/2$ away from the center are shown as red plus signs and blue plus crosses, respectively. We identified three phases, denoted by the vertical dashed lines. Phase II is characterized by a steady decrease of V_{cell} (red arrow), an increase in $\langle e_z \rangle$, and faster growth of H than R. (*Inset*) Ratio between growth rates of the cluster height $\dot{H}$ and radius $\dot{R}$ in phases I and II averaged over five samples (error bars correspond to SDs); the red line corresponds to a ratio of 1.

increase in cluster compactness coincides with a steady increase in $\langle e_z \rangle$. Thus, the increase in cell density at the center of the biofilm is tightly coupled to cell reorientation events that vertically align the cells. A faster expansion rate in the cluster height than in the radius occurs immediately after this transition (Fig. 1*G*, *Inset*), showing that biofilm development has changed from 2D growth to 3D expansion. V_{cell} finally plateaus upon entry into stationary phase.

The 2D-to-3D Transition Is Caused by Surface Adhesion. To determine the trigger of the 2D-to-3D biofilm transition and, ultimately, to cell ordering, we inspected the period between phases I and II of the V_{cell} curve from Fig. 1*G*. During this transition, individual cells at the center of the biofilm reorient away from their initial configuration parallel to the surface (Fig. 2*A*). Daughter cells are born from the poles of these reoriented cells and necessarily extend in the third dimension, triggering the formation of the 3D dome. The reorientation event is puzzling, given that *V. cholerae* cells are adhered to the substrate by the matrix protein Bap1 (25, 26). To investigate this phenomenon, we stained living biofilms made from cells carrying a Bap1-3× FLAG fusion in situ with Cy3-congugated anti-FLAG antibody (Fig. 2*B* and Movie S4). The fusion caused no changes in biofilm morphology. Consistent with earlier work (17), the founder cells secrete significant Bap1 that diffuses to cover the surrounding surface. Surprisingly, in the mature biofilm, Bap1 remains surface-bound, whereas the cells have been lifted up away from the surface, suggesting that a mechanical force overcomes cell-Bap1 bonds to enable cells to reorient vertically.

To represent the biofilm growth process in silico and uncover the forces underlying the cell reorientation events, we developed an agent-based simulation of biofilm formation that incorporates rod-shaped bacteria with and without cell-to-surface bonds (27, 28) (Fig. 2 *C* and *D* and Movie S5). We begin the simulation with a founder cell oriented parallel to the surface. Descendent cells lacking surface attachment spread out along the surface but remain in two dimensions. Cells at the periphery tend to orient tangential to the cluster edge due to being pushed by cells inside the cluster (29). However, when surface attachment is added to the simulation, rim cells maintain their radial orientation throughout growth, reproducing the experimental observation. The central cells, by contrast, are forced to tilt into the third dimension when their surface-adhesion bonds at one pole are overpowered by the total mechanical forces exerted by surrounding cells lying flat on the surface. Reoriented cells automatically extend their subsequent descendants further into the vertical dimension. The agent-based simulations reveal the dual role of cell-to-substrate adhesion: It provides a biophysical mechanism for cells first to attach to the surface and second to reorient and undergo 3D growth as cell density increases. The simulation is not intended to reproduce the complete nematic ordering that occurs in mature biofilms, because we have not yet implemented other matrix components (RbmA and Vps).

We hypothesized that the same surface-associated compression that reorients the cells during growth is responsible for the nematic ordering observed in mature biofilms. To test this hypothesis, we generated deletions of the genes encoding the proteins

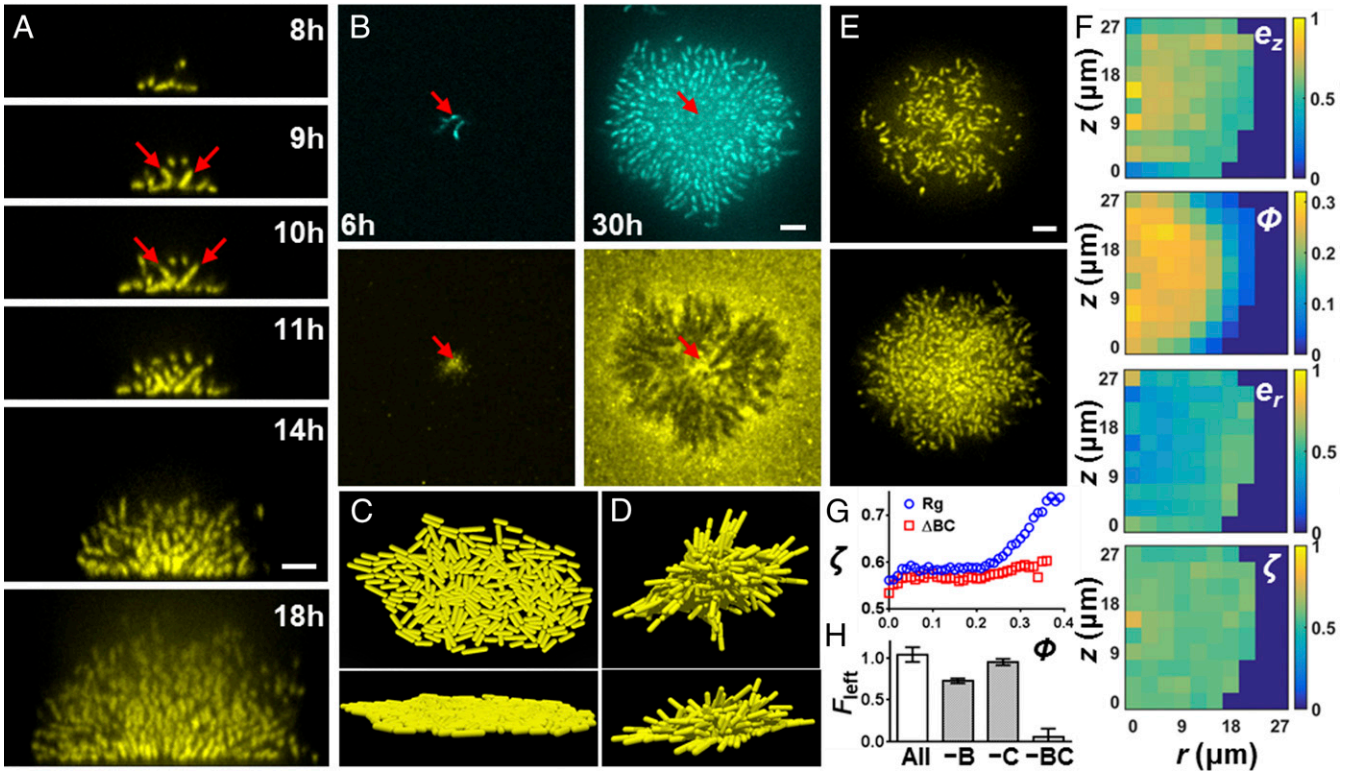

Fig. 2. Cell reorientation and ordering require surface adhesion. (*A*) Side view of a growing biofilm cluster of *V. cholerae* at the indicated times. Red arrows indicate the reoriented cells, as well as their daughter cells. (*B*) Growing *V. cholerae* cluster (*Top*) with Bap1 labeled with Cy3 antibody (*Bottom*) at 6 and 30 h. Arrows indicate the position of the founder cell. (*C* and *D*) Top and side views of a simulated biofilm without (*C*) and with (*D*) cell-to-surface attachment. (*E*) Representative biofilm cluster from Δ*bap1*Δ*rbmC* cells at 18 h at the bottom layer (*Top*) and 5 μm above the surface (*Bottom*). (*F*) Plots of e_z, e_r, ϕ, and ζ for the image shown in *E*. (*G*) Local order parameter $\zeta(\phi)$ versus ϕ for the Rg parent strain (blue circles) and Δ*bap1*Δ*rbmC* (Δ*BC*, red squares). (*H*) Restoration of cell-to-surface attachment in Δ*bap1*Δ*rbmC* biofilms by cell-free conditioned medium lacking the indicated component(s). B denotes Bap1, and C denotes RbmC. Surface attachment is quantified by the fraction of biomass remaining after being subjected to flow (F_{left}), averaged over four biological replicates (error bars correspond to SDs). (Scale bars: *A*, *B*, and *E*, 5 μm.)

responsible for cell-to-surface adhesion. Single mutants of Δ*bap1* and Δ*rbmC* exhibit the same biofilm development pattern as the parent (Fig. S3), consistent with the partially redundant roles of Bap1 and RbmC in mediating cell-to-surface adhesion (17) (Fig. S4). Clusters of the double Δ*bap1*Δ*rbmC* mutant, however, adopt roughly spherical shapes and float above the surface (Fig. 2*E* and Movie S6), consistent with surface attachment being eliminated. A remarkable feature of the Δ*bap1*Δ*rbmC* double-mutant biofilm is that it has also completely lost cell ordering (Fig. 2*F*): No vertically or radially ordered region can be identified. Indeed, neighboring cell orientation is uncorrelated, even though cells remain connected to one another by RbmA (Fig. S4). The disorder is not simply caused by a reduction in biofilm density: Fig. 2*G* shows that for the parent strain, higher local volume fraction is correlated with a stronger local alignment, whereas this trend is abolished in the Δ*bap1*Δ*rbmC* double mutant. Coating the surface with exogenous Bap1 and/or RbmC restores cell-to-surface attachment to the Δ*bap1*Δ*rbmC* biofilms, as well as partially restoring cell ordering (Fig. 2*H* and Fig. S5). Therefore, we conclude that the nematic cell ordering inside biofilms is also a surface-associated phenomenon, likely caused by the same growth-induced surface compression that continuously realigns and packs cells in the vertical direction.

Cell-to-Cell Adhesion Controls the Biofilm Growth Mode. We next investigated the role of cell-to-cell adhesion, mediated by the matrix protein RbmA (17, 30, 31), in shaping biofilm architecture. Fig. 3*A* shows a representative image of the bottom layer of a Δ*rbmA* mutant biofilm cluster, showing much larger cell-to-cell distances than in the parent. The most striking difference in overall biofilm morphology relative to the parent strain is the much reduced cell density in the structure at increasing distance

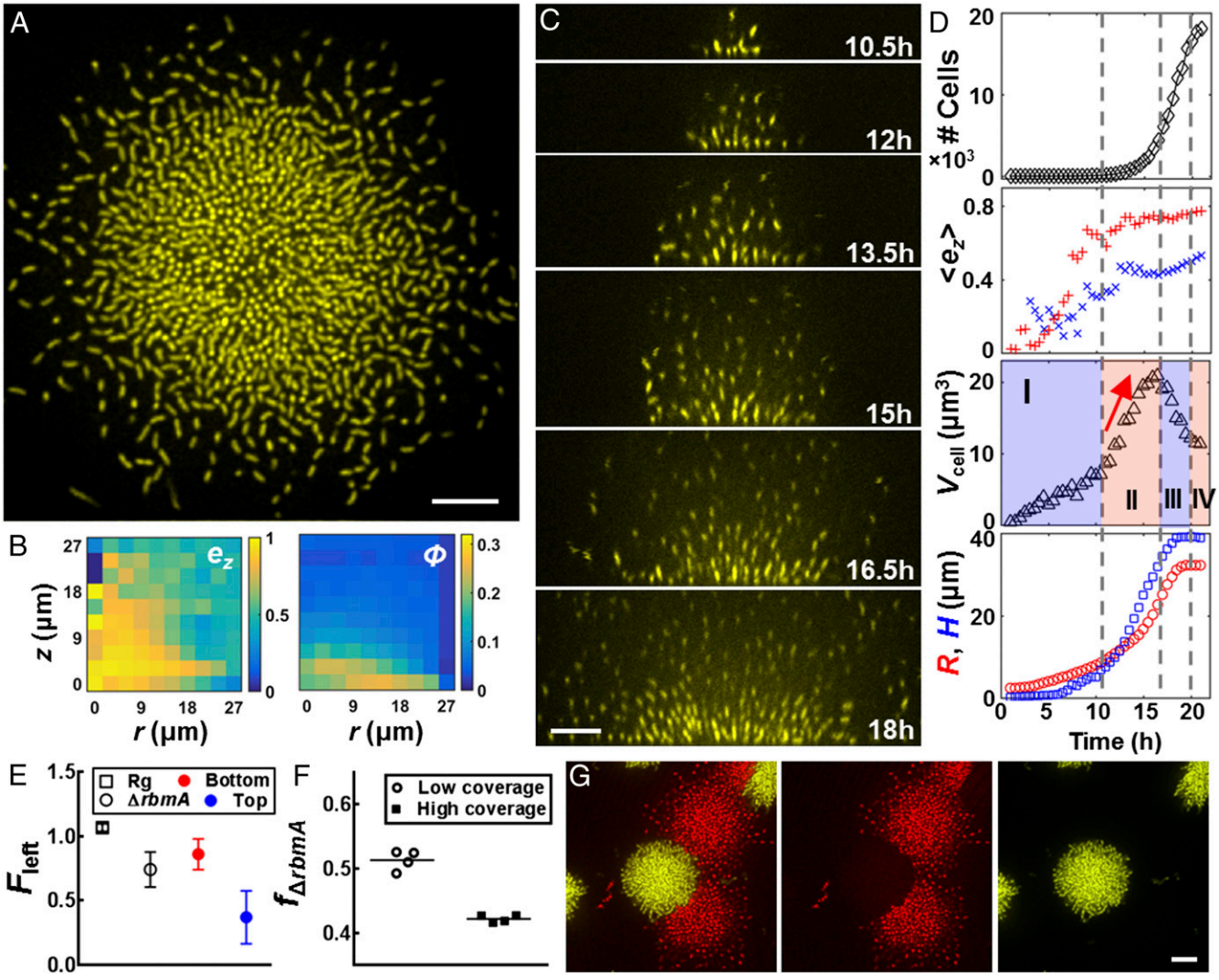

Fig. 3. Deletion of RbmA causes biofilm expansion driven by matrix production. (*A*) Cross-sectional image of the bottom layer of a biofilm cluster of Δ*rbmA* cells at 18 h. (*B*) Corresponding spatial distribution of e_z and ϕ. (*C*) Side view of formation of the Δ*rbmA* biofilm cluster at indicated times. (*D*) Time evolution of cell number, $\langle e_z \rangle$, V_{cell}, *R*, and *H* for the Δ*rbmA* biofilm cluster shown in *C* and *D*. Color and symbol designations follow Fig. 1. V_{cell} shows an additional phase in which V_{cell} increases sharply (red arrow), characterizing the expansion mode driven by the matrix. (*E*) Fraction of cells remaining following mechanical perturbation (F_{left}) for the Rg parent biofilm (□) and the Δ*rbmA* biofilm (○) averaged over four biological replicates (error bars correspond to SDs). For Δ*rbmA* biofilms, we characterize F_{left} for the bottom 75% (red) and top 25% (blue) biofilm biomasses, respectively. (*F*) Final fraction of the Δ*rbmA* mutant remaining ($f_{\Delta rbmA}$) starting from a 1:1 mixture of the Rg parent strain and the Δ*rbmA* mutant at the surface with low surface coverage (○) and high surface coverage (■). (*G*) Representative contact configuration between an Rg biofilm cluster (yellow) and a Δ*rbmA* mutant cluster (red), shown with two channels combined (*Left*) and separated (*Center* and *Right*). (Scale bars: *A*, *C*, and *G*, 10 μm.)

from the substrate, quantitatively shown in Fig. 3*B* by the ϕ plot. We note that degradation or down-regulation of RbmA is not responsible for the ordered packing in the parent (Fig. S6). The time evolution of the Δ*rbmA* mutant biofilm cluster development is shown in Fig. 3*C* and Movies S7 and S8. Following the reorientation transition in the bottom layer of cells, the Δ*rbmA* mutant "explodes" into the third dimension insofar as newly born daughter cells immediately move away from the substrate, maintaining their vertical orientation and leaving behind the surface-attached mother cells. The mature Δ*rbmA* mutant biofilm hence harbors a much larger region of vertically oriented cells than the parent, as characterized by high local e_z (Fig. 3 *B* and *D*).

We suggest that the absence of cell-to-cell adhesion in the Δ*rbmA* mutant allows biofilm expansion mediated by the polymer matrix. Specifically, subsequent to the reorientation events at the surface, the polymer matrix is able to fill the spaces between Δ*rbmA* mother and daughter cells and, in so doing, to carry cells upward, away from the surface. This transport process underpins the dramatic contrast in V_{cell} between the Δ*rbmA* mutant and the parent strain. Whereas in the parent Rg strain, the cluster becomes more dense following the reorientation transition, and thus V_{cell} decreases, in the Δ*rbmA* mutant, V_{cell} increases sharply due to the rapid expansion into the third dimension.

Mechanical Advantages of a Dense Biofilm. We hypothesize that the compact structure of the parent biofilm makes the overall biofilm more resistant to mechanical disruption, perhaps enhancing its stability in the environment. To test this idea, we subjected the different *V. cholerae* biofilms to mechanical agitation (*SI Materials and Methods*). The Rg parent biofilm maintained full integrity after vigorous shaking, whereas the Δ*rbmA* mutant biofilm lost about one-fourth of its original biomass (Fig. 3*E*). Furthermore, biomass was lost primarily from the top layers, the region in which the Δ*rbmA* mutant biofilm has low local cell density (Fig. 3*B*).

To assess the consequences of the loss of RbmA on biofilm mechanical properties further, we performed a biofilm competition assay between the Δ*rbmA* mutant and the parent strain (*SI Materials and Methods*). At a 50:50 starting ratio and at low initial surface coverage (Fig. S7), the two strains had nearly the same fitness (Fig. 3*F*). However, at high surface coverage, where biofilms of different strains are expected to collide and compete for space (32), the Δ*rbmA* mutant is at a disadvantage (the final frequency of the Δ*rbmA* strain, $f_{\Delta rbmA} = 0.42$ after 1 d of biofilm growth). Specifically, the Δ*rbmA* mutant is outcompeted at the bottom layer so much that its access to the third dimension is inhibited (Fig. S7). Although, in principle, the Δ*rbmA* mutant could extend further into the third dimension and access additional nutrients at later stages of biofilm growth as suggested by simulations (9), we do not observe such a reversal of fitness. Hence, we conclude that, under our conditions, competition for space is the overriding factor that determines the outcome of the competition.

The interface between an Rg parent biofilm cluster and a Δ*rbmA* mutant cluster exemplifies the mechanical differences between the strains (Fig. 3*G*). The hemispherical shape of the parent biofilm cluster is minimally perturbed by the presence of the colliding Δ*rbmA* mutant cluster, whereas the Δ*rbmA* mutant cluster is deformed by the colliding parent biofilm cluster. By contrast, collisions between two Rg biofilm clusters or two Δ*rbmA* biofilm clusters result in straight boundaries (Fig. S8). Furthermore, isolated clusters of the parent strain are able to expand laterally even if embedded within Δ*rbmA* mutant biofilms (Fig. S8). Hence, we conclude that the dense growth mode driven by bacterial proliferation, rather than matrix expansion, endows *V. cholerae* biofilms with strong mechanical properties, and consequently provides an evolutionary advantage so that they can withstand environmental perturbations, such as shear flow, mechanical shock, or competition with other biofilm-forming species.

The *V. cholerae* Biofilm Development Program. Our results suggest the following model for the *V. cholerae* biofilm structural development program (Fig. 4). Following attachment to the surface, the founder cell orients horizontally to maximize cell-to-surface adhesion, which is mediated by Bap1/RbmC. Subsequent divisions oriented along the long axes of the rod-shaped cells confine the early descendants to the same plane as the founder cell, resulting in a relatively flat colony. During midexponential growth, cells proliferate rapidly but their expansion in space is restricted by the surface-attached, peripheral cells. The combination of expansion and confinement generates an effective anisotropic stress that overpowers the cell-to-surface adhesion force for cells at the cluster center, causing these cells to realign in the vertical direction and triggering the transition from 2D expansion to 3D growth. The modestly curved shape of *V. cholerae* might further facilitate such reorientation events. Similar compression-driven reorientation is observed in bacterial colony growth confined between agar and glass (29, 33); in the current context, we show the biological relevance of this transition for natural biofilm growth. The descendants of the reoriented cells remain connected to one another at their poles by RbmA (17), so local proliferation leads to a steady increase in cell density. The increased density translates into an enhanced compression that gradually packs the central core of the cluster into a nematically ordered state with the rod-like cells all oriented perpendicular to the surface, which further amplifies the anisotropic growth of the biofilm in the vertical direction. In this growth mode, biofilm expansion is primarily driven by the directional proliferation of the bacterial cells themselves. The production of extracellular polymer could, in principle, expand the biofilm; however, such expansion is resisted by the cell-to-cell connections. By contrast, in the Δ*rbmA* mutant, the absence of cell-to-cell linkages switches the biofilm growth mode to one that is mainly driven by matrix expansion, leading to an overall larger,

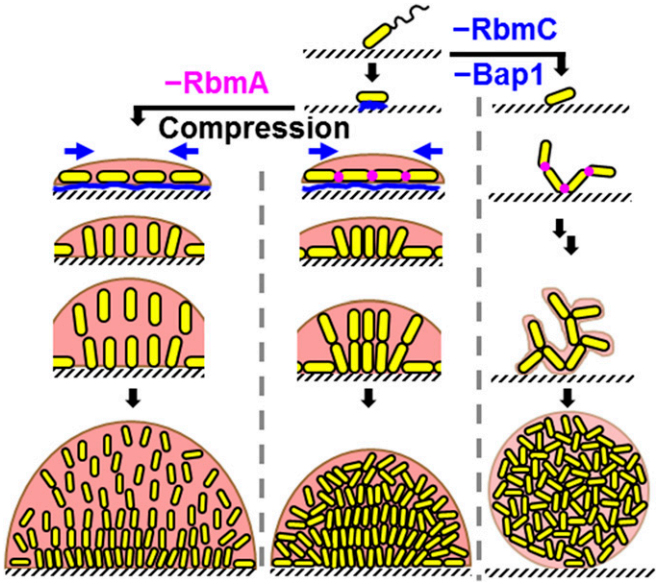

Fig. 4. Schematic representation of the *V. cholerae* biofilm formation process. Yellow cylinders represent the rod-shaped bacterial cells. Blue represents the RbmC/Bap1 matrix proteins that adhere the cells to the surface. Magenta denotes the RbmA protein. The pale peach background represents the Vps matrix, and its transparency in the different panels corresponds to the amount of Vps present in the biofilm. The brown contour at the rim of the biofilms represents the envelope formed by Vps/RbmC/Bap1. Blue arrows denote the spontaneously generated, surface-associated compression that is responsible for cell reorientation and ordering.

but much looser, biofilm. The absence of cell-to-surface adhesion in the Δ*bap1*Δ*rbmC* mutant enables the cells to grow away from the surface, but without any surface-mediated compression, the biofilm remains disordered. In essence, *V. cholerae* has evolved specific matrix proteins with properties that allow it to harness the consequent biophysical processes to achieve a 3D, strong, and ordered biofilm structure that firmly attaches to surfaces. Indeed, underproduction or overproduction of any of these three crucial proteins inhibits proper development of the biofilm structure (Fig. S9). For example, overexpression of Bap1 leads to enhanced attachment of cells to the surface, which impedes the transition into the third dimension.

Our findings regarding the *V. cholerae* biofilm developmental process invite interesting comparisons with other biofilm-forming bacterial species. We provide two here. For species with surface twitching motility, such as *Pseudomonas aeruginosa*, it is conceivable that surface-associated pressure might be relieved by surface motion, and, indeed, aggregation of motile *P. aeruginosa* is suggested to initiate biofilm formation rather than clonal growth from a single cell (13). However, in later stages of the process, a nonmotile subset of the *P. aeruginosa* cells forms the 3D stalk at the base of the biofilm (34). The stalk formation process could nonetheless involve reorientation-extension events similar to those events discovered here. Spherical bacteria, such as *Staphylococcus aureus*, pose a different challenge for 3D biofilm development. Despite their isotropic shape, cocci divide sequentially in orthogonal planes (35). It remains to be discovered how such directional division drives 3D growth for cocci biofilms, especially in cases of cocci, such as *S. aureus*, that possess low levels of extracellular polysaccharide. Such systems can now be readily accessed using the technology presented in this study.

In conclusion, with our live, single-cell resolution imaging and analysis protocol, we discovered the key structural transitions in the developmental process of *V. cholerae* biofilms, as well as the underlying biophysical and genetic principles. Going forward, our single-cell imaging technology enables screening for genes that affect fine features of biofilms not resolvable by traditional assays, such as crystal-violet staining (36), colony morphology descriptions, or overall biomass quantification. Further increasing the spatial and temporal resolution of the technology will enable tracking of cell shape, size, and lineage to address the cell biological processes (37) occurring inside bacterial biofilms. Finally, we envision extending our single-cell biofilm analyses to gene expression to assess cell-to-cell heterogeneity (38, 39) in response to stimuli that include antibiotics, signal molecules, and nutrient limitation.

Materials and Methods

Strains and Media. All *V. cholerae* strains used in this study are derivatives of the wild-type *V. cholerae* O1 biovar El Tor strain C6706, harboring a missense mutation in the *vpvC* gene (VpvC W240R) that elevates c-di-GMP levels, conferring an Rg biofilm phenotype (23). Additional mutations were engineered into this *V. cholerae* strain using *Escherichia coli* S17-λ*pir* carrying pKAS32. All strains were grown in LB at 37 °C with shaking. Biofilm experiments were performed in M9 minimal medium, supplemented with 2 mM $MgSO_4$, 100 μM $CaCl_2$, and 0.5% glucose. A detailed strain list is provided in Table S1.

Biofilm Growth. *V. cholerae* strains were grown overnight at 37 °C in liquid LB with shaking, back-diluted 30-fold, and grown for an additional 2 h with shaking in M9 medium until early exponential phase (OD_{600} = 0.1–0.2). For time course biofilm imaging, these regrown cultures were diluted to OD_{600} = 0.001 and 100 μL of the diluted cultures was added to wells of 96-well plates with no. 1.5 coverslip bottoms (MatTek). The cells were allowed to attach for 10 min, after which the wells were washed twice with fresh M9 medium and, subsequently, 100 μL of fresh M9 medium was added. The low initial inoculation density enabled isolated biofilm clusters to form. The locations of the founder cells were identified, and 1 h after inoculation, imaging was begun on the microscope stage at 25 °C. For non-time course experiments, the inoculated plates were incubated at 30 °C for 16–18 h before imaging.

Microscopy. Images were acquired with a Yokogawa CSU-X1 confocal spinning disk unit mounted on a Nikon Ti-E inverted microscope, using a 60× water objective with a numerical aperture of 1.2, a 543-nm laser (OEM DPSS), and an Andor iXon 897 EMCCD camera. The water objective was crucial to minimize the refractive index mismatch and resulting spherical aberration, which elongates objects, especially for those objects most distant from the surface. To avoid evaporation, immersion oil with a refractive index of 1.3300 ± 0.0002 (Cargille) was used instead of water. To obtain sufficient magnification for automated cell segmentation, a 1.5× lens was placed between the CSU-X1 unit and the Nikon Ti-E side port. The distances between the spinning disk, the tube lens, and the camera sensor were adjusted to provide optimal *z* resolution. The magnification was 166 nm per pixel in the *x*–*y* plane, with a 200-nm step size in the *z* direction. The point spread function (PSF) of the system was measured under identical conditions (with a 50-nm *z*-step size) using 200-nm fluorescent polystyrene beads (ex540/em561; Life Technologies). The time difference between each image acquisition was 30 min, and the total acquisition time was 20 h for each experiment. To decrease photodamage to the cells further, an adaptive *z* range was used: 5 μm for the first 5 h, 15 μm for the next 5 h, and 25 μm for the final 10 h. For the Rg strain, this strategy captured at least 98% of the cells, including those cells in the tallest clusters. For the Δ*bap1*Δ*rbmC* and Δ*rbmA* mutants, we increased the *z* range accordingly. All image acquisitions were automated using Nikon Element software. All experimental images in this work are raw images from this step, rendered by Nikon Element software.

Deconvolution and Image Processing. The PSF of the system was distilled with Huygens Professional software (SVI). Raw image data were deconvolved using the distilled PSF. To segment the biofilms into individual cells from 3D images, custom code was written in MATLAB (MathWorks). First, a 3D watershed algorithm was applied to the *z* stacks to separate objects in close proximity to one another. Next, automatic thresholding was independently applied to each layer to account for the decreasing signal with *z* height. Subsequently, binary objects were connected between the different *z* planes to obtain 3D volumes for each cell inside the biofilm. The orientation of each cell was next extracted as the first principal component in the principal component analysis of the *x*, *y*, and *z* coordinates for all voxels present in each cell. *V. cholerae* cells have a slightly curved shape; however, for simplicity, we modeled and tracked the cells as rods. A discussion of the core MATLAB code is available in *SI Materials and Methods*.

ACKNOWLEDGMENTS. We thank Dr. Knut Drescher for help in image analysis and Dr. Carey Nadell for help with strain construction. We thank them and the members of the B.L.B. laboratory for helpful discussions. We thank Dr. Gary Laevsky and the Confocal Microscopy Facility (a Nikon Center of Excellence) for help with optics. This work was supported by the Howard Hughes Medical Institute, NIH Grant 5R01GM065859, National Science Foundation Grant MCB-0948112 (to B.L.B.), and National Science Foundation Grant MCB-1344191 (to N.S.W., B.L.B., and H.A.S.).

1. Hall-Stoodley L, Costerton JW, Stoodley P (2004) Bacterial biofilms: From the natural environment to infectious diseases. *Nat Rev Microbiol* 2(2):95–108.
2. Flemming HC, Wingender J (2010) The biofilm matrix. *Nat Rev Microbiol* 8(9): 623–633.
3. Ghannoum M, Parsek M, Whiteley M, Mukherjee PK (2015) *Microbial Biofilms* (ASM Press, Washington, DC), 2nd Ed.
4. Costerton JW, Stewart PS, Greenberg EP (1999) Bacterial biofilms: A common cause of persistent infections. *Science* 284(5418):1318–1322.
5. Mah TF, et al. (2003) A genetic basis for *Pseudomonas aeruginosa* biofilm antibiotic resistance. *Nature* 426(6964):306–310.
6. Drescher K, Shen Y, Bassler BL, Stone HA (2013) Biofilm streamers cause catastrophic disruption of flow with consequences for environmental and medical systems. *Proc Natl Acad Sci USA* 110(11):4345–4350.
7. Nerenberg R (2016) The membrane-biofilm reactor (MBfR) as a counter-diffusional biofilm process. *Curr Opin Biotechnol* 38:131–136.
8. Hobley L, Harkins C, MacPhee CE, Stanley-Wall NR (2015) Giving structure to the biofilm matrix: An overview of individual strategies and emerging common themes. *FEMS Microbiol Rev* 39(5):649–669.
9. Xavier JB, Foster KR (2007) Cooperation and conflict in microbial biofilms. *Proc Natl Acad Sci USA* 104(3):876–881.
10. Alpkvist E, Picioreanu C, van Loosdrecht MCM, Heyden A (2006) Three-dimensional biofilm model with individual cells and continuum EPS matrix. *Biotechnol Bioeng* 94(5):961–979.
11. Keller PJ, Schmidt AD, Wittbrodt J, Stelzer EHK (2008) Reconstruction of zebrafish early embryonic development by scanned light sheet microscopy. *Science* 322(5904): 1065–1069.

12. Neu TR, et al. (2010) Advanced imaging techniques for assessment of structure, composition and function in biofilm systems. *FEMS Microbiol Ecol* 72(1):1–21.
13. Zhao K, et al. (2013) Psl trails guide exploration and microcolony formation in *Pseudomonas aeruginosa* biofilms. *Nature* 497(7449):388–391.
14. Serra DO, Richter AM, Klauck G, Mika F, Hengge R (2013) Microanatomy at cellular resolution and spatial order of physiological differentiation in a bacterial biofilm. *mBio* 4(2):e00103–e00113.
15. Nelson EJ, Harris JB, Morris JG, Jr, Calderwood SB, Camilli A (2009) Cholera transmission: The host, pathogen and bacteriophage dynamic. *Nat Rev Microbiol* 7(10): 693–702.
16. Teschler JK, et al. (2015) Living in the matrix: Assembly and control of *Vibrio cholerae* biofilms. *Nat Rev Microbiol* 13(5):255–268.
17. Berk V, et al. (2012) Molecular architecture and assembly principles of *Vibrio cholerae* biofilms. *Science* 337(6091):236–239.
18. Krasteva PV, et al. (2010) *Vibrio cholerae* VpsT regulates matrix production and motility by directly sensing cyclic di-GMP. *Science* 327(5967):866–868.
19. Hammer BK, Bassler BL (2003) Quorum sensing controls biofilm formation in *Vibrio cholerae*. *Mol Microbiol* 50(1):101–104.
20. Drescher K, et al. (2016) Architectural transitions in *Vibrio cholerae* biofilms at single-cell resolution. *Proc Natl Acad Sci USA* 113(14):E2066–E2072.
21. Stewart EJ, Satorius AE, Younger JG, Solomon MJ (2013) Role of environmental and antibiotic stress on *Staphylococcus epidermidis* biofilm microstructure. *Langmuir* 29(23):7017–7024.
22. Karasawa S, Araki T, Nagai T, Mizuno H, Miyawaki A (2004) Cyan-emitting and orange-emitting fluorescent proteins as a donor/acceptor pair for fluorescence resonance energy transfer. *Biochem J* 381(Pt 1):307–312.
23. Beyhan S, Yildiz FH (2007) Smooth to rugose phase variation in *Vibrio cholerae* can be mediated by a single nucleotide change that targets c-di-GMP signalling pathway. *Mol Microbiol* 63(4):995–1007.
24. Volfson D, Cookson S, Hasty J, Tsimring LS (2008) Biomechanical ordering of dense cell populations. *Proc Natl Acad Sci USA* 105(40):15346–15351.
25. Fong JC, Yildiz FH (2007) The *rbmBCDEF* gene cluster modulates development of rugose colony morphology and biofilm formation in *Vibrio cholerae*. *J Bacteriol* 189(6):2319–2330.
26. Absalon C, Van Dellen K, Watnick PI (2011) A communal bacterial adhesin anchors biofilm and bystander cells to surfaces. *PLoS Pathog* 7(8):e1002210.
27. Lardon LA, et al. (2011) iDynoMiCS: Next-generation individual-based modelling of biofilms. *Environ Microbiol* 13(9):2416–2434.
28. Álvarez JPA, Aradas ARP (2012) Enhancing iDynoMiCS framework to simulate rod-shape bacterial colonies growth. Available at www.lia.upm.es/index.php/simulators/idynomics. Accessed July 2, 2015.
29. Su PT, et al. (2012) Bacterial colony from two-dimensional division to three-dimensional development. *PLoS One* 7(11):e48098.
30. Fong JC, Karplus K, Schoolnik GK, Yildiz FH (2006) Identification and characterization of RbmA, a novel protein required for the development of rugose colony morphology and biofilm structure in *Vibrio cholerae*. *J Bacteriol* 188(3):1049–1059.
31. Maestre-Reyna M, Wu WJ, Wang AH (2013) Structural insights into RbmA, a biofilm scaffolding protein of *V. cholerae*. *PLoS One* 8(12):e82458.
32. Schluter J, Nadell CD, Bassler BL, Foster KR (2015) Adhesion as a weapon in microbial competition. *ISME J* 9(1):139–149.
33. Grant MA, Wacław B, Allen RJ, Cicuta P (2014) The role of mechanical forces in the planar-to-bulk transition in growing *Escherichia coli* microcolonies. *J R Soc Interface* 11(97):20140400.
34. Parsek MR, Tolker-Nielsen T (2008) Pattern formation in *Pseudomonas aeruginosa* biofilms. *Curr Opin Microbiol* 11(6):560–566.
35. Monteiro JM, et al. (2015) Cell shape dynamics during the staphylococcal cell cycle. *Nat Commun* 6:8055.
36. O'Toole GA (2011) Microtiter dish biofilm formation assay. *J Vis Exp* 47:e2437.
37. Cabeen MT, Jacobs-Wagner C (2005) Bacterial cell shape. *Nat Rev Microbiol* 3(8):601–610.
38. Stewart PS, Franklin MJ (2008) Physiological heterogeneity in biofilms. *Nat Rev Microbiol* 6(3):199–210.
39. Wessel AK, Hmelo L, Parsek MR, Whiteley M (2013) Going local: Technologies for exploring bacterial microenvironments. *Nat Rev Microbiol* 11(5):337–348.
40. Smith DR, et al. (2015) In situ proteolysis of the *Vibrio cholerae* matrix protein RbmA promotes biofilm recruitment. *Proc Natl Acad Sci USA* 112(33):10491–10496.
41. Thelin KH, Taylor RK (1996) Toxin-coregulated pilus, but not mannose-sensitive hemagglutinin, is required for colonization by *Vibrio cholerae* O1 El Tor biotype and O139 strains. *Infect Immun* 64(7):2853–2856.
42. Skorupski K, Taylor RK (1996) Positive selection vectors for allelic exchange. *Gene* 169(1):47–52.
43. Nadell CD, Drescher K, Wingreen NS, Bassler BL (2015) Extracellular matrix structure governs invasion resistance in bacterial biofilms. *ISME J* 9(8):1700–1709.
44. Drescher K, Nadell CD, Stone HA, Wingreen NS, Bassler BL (2014) Solutions to the public goods dilemma in bacterial biofilms. *Curr Biol* 24(1):50–55.